Magnetic properties of 4f adatoms on graphene: Density functional theory investigations

Johanna P. Carbone [1,2,*] Juba Bouaziz [1] Gustav Bihlmayer [1] and Stefan Blügel [1]

[1]*Peter Grünberg Institut and Institute for Advanced Simulation, Forschungszentrum Jülich and JARA, 52425 Jülich, Germany*

[2]*Physics Department, RWTH-Aachen University, 52062 Aachen, Germany*

(Received 26 June 2023; revised 29 September 2023; accepted 1 November 2023; published 20 November 2023)

Rare-earth atoms on top of 2D materials represent an interesting platform with the prospect of tailoring the magnetic anisotropy for practical applications. Here, we investigate the ground state and magnetic properties of selected 4f atoms deposited on a graphene substrate in the framework of the DFT + U approach. The inherent strong spin-orbit interaction in conjunction with crystal field effects acting on the localized 4f shells results in a substantial magnetic anisotropy energy (tens of meVs), whose angular dependence is dictated by the C_{6v} symmetry of the graphene substrate. We obtain the crystal-field parameters and investigate spin-flip events via quantum tunneling of magnetization in the view of achieving a protected quantum-spin behavior. Remarkably, the large spin and orbital moments of the open 4f shells (Dy, Ho, and Tm) generate a strong magnetoelastic coupling which provides more flexibility to control the magnetic state via the application of external strain.

DOI: 10.1103/PhysRevB.108.174431

I. INTRODUCTION

Graphene (Gr) was the first 2D material to be discovered and stimulated interest at the technological and fundamental research levels. A multitude of fascinating electronic phenomena can be tailored in different 2D materials by tuning the chemical composition and structural properties [1–6]. The experimental realization of these nanostructured systems might lead to the next generation of efficient spintronics devices [7]. In this material class, magnetic rare-earth (R) atoms deposited on surfaces represent a promising pathway to achieve magnetic remanence and hence design stable memory devices. The R localized 4f electrons carry large spin and orbital moments, generating strong spin-orbit coupling (SOC) effects [8] and magnetocrystalline anisotropy, which, combined with a relatively low magnetic damping [9] results in stable nanometric scale magnets. More exotic magnetic phenomena can be generated and controlled when these R atoms are deposited on 2D materials.

Also, at the experimental level, single-ion magnets deposited on top of 2D-material substrates are under scrutiny. These might serve as building blocks for quantum computer "qubits," where the central desired property is a long coherence time, which translates into a large magnetic anisotropy in conjunction with a low damping of the magnetic excitations, thus reducing the quantum fluctuation [10,11]. This raises the prospect of employing the 4f elements as a quantistic information carrier [12,13], since the magnetic unit emerges from strongly localized 4f electrons, well separated from the surrounding itinerant spd-electron cloud. In fact, the chemical and magnetic interactions of R atoms on 2D materials, and how to exploit the protection of R atoms from quantum tunneling of magnetization, are currently attracting a lot of attention [14–19]. Specifically, combining scanning tunneling microscopy with x-ray magnetic circular dichroism (XMCD) measurements allows for the determination of adsorption, chemical diffusion, and orbital occupation characteristics of individual R atoms on the 2D material. By recording the XMCD signal while varying the external magnetic field, it is possible to reveal magnetic hysteresis, shedding light on magnetic anisotropy properties. These properties are further analyzed using multiplet calculations to assess magnetic stability from a quantum perspective [20–26].

For practical applications, tailoring the magnetic anisotropy is a fundamental aspect. For instance, Herman *et al.* [27] investigated the possibility of modifying the magnetic anisotropy of a Dy/Ir surface alloy by a lifting skyhook effect of the Dy atoms from the Ir surface when brought in contact with a graphene sheet. Here, the fd hybridization of the Dy electrons generates long tails of the charge distribution that overlap with the Ir(111) orbitals. When graphene is deposited on top of Dy/Ir(111), the fd states of Dy also hybridize with the π orbitals arising from the carbon structure, and this interaction results in an increased separation of the Dy atoms from the Ir(111) surface due to the Dy-Gr interaction. This effect leads to a redistribution of the charge density that enhances the magnetic anisotropy.

Concerning single R atoms on surfaces, a graphene sheet is often introduced as a decoupling layer between a metallic or insulating surface and the R atoms to decouple the magnetic source from any possible scattering events, for example, of conduction electrons or phonons. In addition, graphene presents a C_{6v} symmetry which can be exploited to tune the quantum states of the R atom to achieve further stabilization of the magnetization, since the respective hexagonal crystal field (CF) removes the degeneracy of the magnetic states in a free atom and thus can generate an energy dispersion that is protected against magnetization reversal. This magnetic stabilization strictly depends on the properties of the chosen R

*j.carbone@fz-juelich.de

atom, i.e., its orbital and spin angular momentum, which are coupled by the SOC that determines the number and nature of magnetic states interacting with the CF.

Recently, several theoretical investigations have been carried out. From this perspective, the presence of strongly localized $4f$ orbitals enhances the complexity of first-principles approaches, since common approximations to describe the exchange and correlation energy such as local density approximations (LDAs) fail to provide an accurate description. To properly account for the strong Coulomb effects in the $4f$ atoms, methods going beyond the standard approximations to density functional theory (DFT), including strongly correlated electron methods such as the Hubbard-I approximation [28–31] or dynamical mean-field theory [32], are often adopted. A simpler alternative for the treatment of $4f$ electrons is the LDA + U approach [33], which incorporates the local Coulomb repulsion in the form of a Hubbard correction in addition to the LDA exchange-correlation.

In the present paper, we perform an analysis of magnetic properties of three heavy R atoms, namely Dy, Ho, and Tm. The choice of these candidates is motivated by preceding experimental investigations [15,17,20,23–25]. Using a supercell approach, we determine the electronic structure of these $4f$ atoms deposited on a free-standing graphene sheet. We employ the GGA + U method parameterized following the formulation of Ref. [34]. The magnetic anisotropy constants are determined by fitting the total energy for different magnetization orientations relative to the crystal lattice. We then propose an analytical method which permits us to reverse engineer the crystal field parameters (CFPs) from the anisotropy constants. The calculated CFPs are employed to construct the C_{6v} CF matrix for each R atom, which is diagonalized to obtain the J_z multiplet spectrum of the R/Gr complexes. We then examine the magnetoelastic coupling in terms of magnetic anisotropy constants by simulating an external stress acting on the samples with magnetizations aligned along different orientations and determine the frequency of the respective vibrational mode. Finally, we underline the importance of an accurate theoretical description of the $4f$ electrons by analyzing deviations of the magnetic anisotropy following different orbital occupations in the $4f$ shell.

II. STRUCTURAL AND ELECTRONIC PROPERTIES

A. Computational details

The presented results are obtained using DFT as implemented within the full-potential-linearized augmented plane wave (FLAPW) method using the FLEUR code [35,36]. All the simulations have been performed in a $\sqrt{3} \times \sqrt{3}$ supercell containing one magnetic atom and six carbon (C) atoms (see Fig. 1), with lattice constant equal to the experimental value of 2.46 Å, respectively, multiplied by $\sqrt{3}$. The selection of the simulation cell is guided by both experimental and theoretical findings, as documented in Refs. [37,38]. These suggest that Eu atoms, which share chemical characteristics with other R elements lacking an external $5d$ electron in the valence shell, tend to form a $\sqrt{3} \times \sqrt{3}$ superstructure on graphene. After the investigation of the magnetoelastic properties of the R atoms in this unit cell, in Sec. VII we will revisit a discussion on the choice of the supercell with respect to the obtained magnetic anisotropy properties.

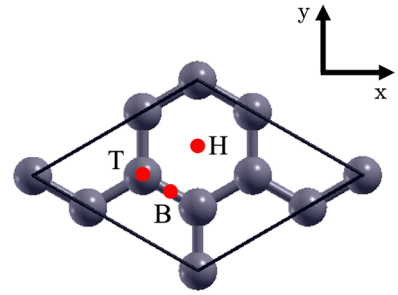

FIG. 1. $\sqrt{3} \times \sqrt{3}$ supercell including six carbon atoms (gray spheres). The three possible adsorption sites of the rare-earth atom on graphene are depicted with red circles named H, T, and B, respectively.

The SOC was incorporated self-consistently adopting the second variation [39] formulation on a 20×20 **k**-point mesh and a cutoff for the plane-wave basis functions of $K_{\max} = 4.5\, a_0^{-1}$ and $G_{\max} = 13.5\, a_0^{-1}$ (a_0 being the Bohr radius). The muffin-tin radii have been set to $2.80\, a_0$ for the R atoms and $1.27\, a_0$ for the C atoms. The upper limit of the angular momentum inside the muffin tin is set to $l_{\max} = 10$ for the R atom and $l_{\max} = 6$ for C. The exchange-correlation potential is taken in the generalized gradient approximation (GGA) following the parametrization PBE [40]. For the R's correlated $4f$ orbitals, a Hubbard correction is applied, both Coulomb U and intratomic exchange interaction J are included, and the double counting is taken in the fully localized limit [34].

We consider three heavy R prototypes, namely, Dy, Ho, and Tm. The values of the DFT + U parameters are set to $U = 7.0,\ 7.03,\ 7.1$ eV and $J = 0.87,\ 0.83,\ 0.86$ eV, respectively. These parameters are chosen following Ref. [29] for Ho and Ref. [30] for Dy. The values for Tm are chosen according to the interpolation formula given in Ref. [41]. Moreover, the values of $U \sim 7$ eV are also chosen on the basis of the work conducted in Ref. [42], where it is shown that it is able to accurately reproduce the electronic and cohesive properties of R bulk systems. We study a situation in which the electrons of the magnetic atoms relax into $4f$ occupations that reflect Hund's rules, i.e., total angular momentum $J = 8$ for Dy, $J = 15/2$ for Ho and $J = 7/2$ for Tm. For these systems on graphene, we assume that Hund's rule dominates over the graphene CF, and therefore an occupation control in combination with the LDA + U approach [43,44] is not further pursued. We note, however, that a deeper analysis shows that for Dy/Gr a solution deviating from Hund's rules with a total angular momentum of $J = 7$ is found to be energetically more favorable. We present a detailed analysis of this state in Sec. VI.

B. Structural details

To identify the lowest energy adsorption site, three possible positions are taken into account: the hollow site (H) at the center of the hexagonal ring, on top of a C atom (T), and in the middle of a C–C bonding (B). These positions are illustrated in Fig. 1 and the respective adsorption energies (in eV) are

TABLE I. Adsorption energies (eV), for the different rare-earth atoms on graphene for each considered adsorption site. The calculations have been performed including SOC self-consistently following the formulation in Eq. (1).

Site	Dy	Ho	Tm
H	−0.545	−0.476	−0.399
T	−0.074	−0.339	−0.280
B	−0.086	−0.344	−0.286

summarized in Table I. The adsorption energies have been obtained considering the total energy difference between the total interacting system and the individual components as

$$E_{\text{ads}} = E_{R/\text{Gr}} - E_R - E_{\text{Gr}} \quad (1)$$

to capture the energy involved in the formation of the complex, compared to the energy of the sum of the isolated R atom and graphene monolayer. In Eq. (1) $E_{R/\text{Gr}}$ is the total energy of the R/Gr complex, while E_R and E_{Gr} correspond to the total energy of the isolated R atom and graphene monolayer, respectively. The results show that for all three R atoms, the H site is energetically the most favorable, in agreement with several other theoretical and experimental studies [15,16,20,24,25,45], and the adatoms on graphene are described by the point group C_{6v}. The bonding strengths appear to be reduced on the T and B sites for Ho and Tm, and negligible for Dy.

In the following, we focus on the H site and perform structural relaxations allowing the 4f atom to adjust its height along the c axis (z direction with respect to the graphene) until reaching minimization of total energy and forces acting on the R atom, with the SOC included self-consistently. The obtained ground-state properties including the f and d occupations, spin, and orbital moments are provided in Table II.

C. Electronic properties

The 5d and 4f occupations shown in Table II clearly show that R atoms undergo a semi-atomic-like behavior, where the 4f shell follows Hund's rules while acquiring some d occupation. This semi-atomic picture can be visualized in the spin-resolved density of states (DOS) shown in Figs. 2(a)–2(c), where the f occupation is shown in red and the d occupation in blue. The DOS of the pristine graphene is given in Fig. 2(d) and is compared to the doped graphene DOS. We only show Ho/Gr as it looks identical for the Dy and Tm impurities. Figure 2(d) shows that the R/Gr systems exhibit a metallic behavior due to the n doping coming from the lanthanide impurities. The magnitude of the doping can be estimated from the energy difference between the pristine graphene and the doped one, which is of the order of 1.4 eV, in agreement with the charge transfer calculations carried out in Ref. [46]. This charge transfer is driven by the hybridization between the graphene p_z orbitals and the magnetic atom's d orbitals.

A clear correlation between the adsorption energies in the H site and the d occupation appears with Dy having the highest d occupation (Table II) and showing also the strongest bonding towards the substrate (Table I). Moreover, we observe that the small bonding energy at the T and B sites discussed previously is reflected in a low d occupation of the R atoms, indicating the major role played by the d electrons in the chemical bonding. The LDOS of the 4f atoms, depicted in Figs. 2(a)–2(c), shows that the f states are hybridized and spread over a large energy window. These states exhibit an insulating character featuring a gap between the occupied and unoccupied states, with the occupied states lying close to the Fermi energy.

TABLE II. Perpendicular distance from the graphene monolayer (Å), d and f occupation, magnetic moment and orbital moment (μ_B) of the rare-earths atoms on graphene in the H site. Calculations have been performed in presence of SOC.

Rare earth	Distance d_0 (Å)	d_{occ}	f_{occ}	m_s^R (μ_B)	m_l^R (μ_B)	m_s^{tot} (μ_B)
Dy	2.49	0.262	9.891	4.040	5.876	4.174
Ho	2.50	0.250	10.881	3.045	5.905	3.150
Tm	2.47	0.237	12.867	1.027	3.000	1.072

D. Magnetic moments

The orbital (m_l^{R}) and spin (m_s^{R}) moments of the R's provided in Table II closely follow Hund's rules. Nonetheless, the m_s^{R} values are slightly higher than the R^{2+} ionic atom case due to the spin polarization of d occupation via an intra-atomic $f-d$ exchange interaction. This d spin polarization is about 0.04 μ_B for Dy, 0.03 μ_B for Ho, and 0.01 μ_B for Tm, respectively. This decay reflects the decreasing value of m_s^{R} from Dy to Tm. The muffin-tin C spin polarization has a very small induced moment of ∼0.001 μ_B. The total magnetic moment of the system m_s^{tot} is naturally dictated by the 4f, which is inversely proportional to the f occupation for late-series R's as shown in Table II. The interstitial region of the structure (space between the atoms) is mostly represented by the delocalized π orbitals of graphene and d electrons of the R atom. These π and d electrons carry a small spin moment $\Delta m = m_s^{\text{tot}} - m_s^{\text{R}}$ induced by the presence of the R atom. The induced magnetization is proportional to the R's atom spin moment and is given by 0.125 μ_B for Dy/Gr, 0.094 μ_B for Ho/Gr, and 0.036 μ_B for Tm/Gr.

III. MAGNETIC ANISOTROPY AND CRYSTAL FIELD COEFFICIENTS

The adsorption of an atom on a surface leads to physical properties that drastically differ from the isolated atom. As the R atoms are in contact with the surface, they experience the electric field produced by the surrounding atomic charges. This CF [47] results in a lowering of the symmetry of the spherical potential in an isolated atom. The form of this field is dictated by the lattice symmetry and local chemical environment and determines the angular dependence of the total energy upon rotation of the magnetization, i.e., the magnetic anisotropy. The conventional anisotropy energy functional describing the angular dependence of the magnetic anisotropy

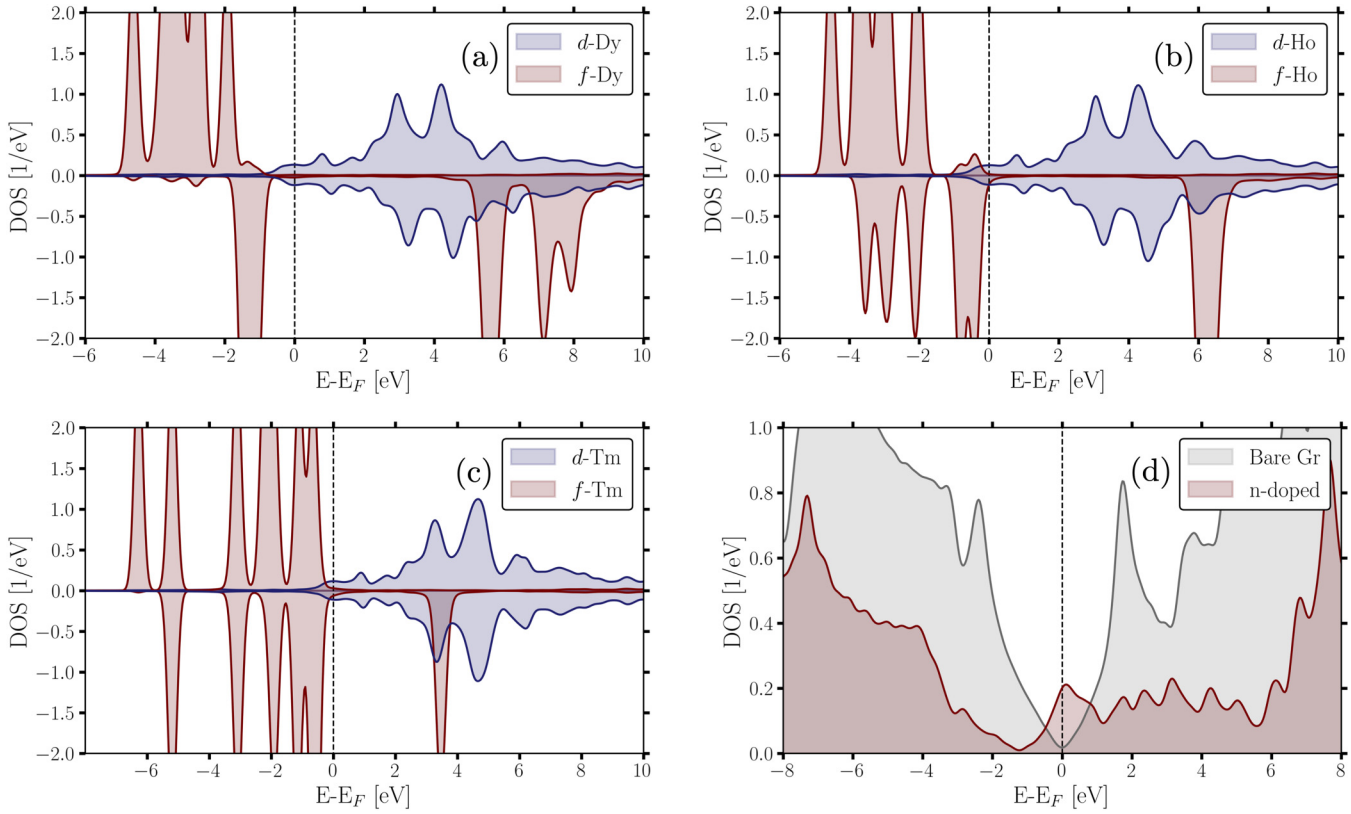

FIG. 2. Spin-polarized density of states of the d (blue) and f (red) electrons of (a) Dy, (b) Ho, and (c) Tm, on top of graphene. The upper half of the plots display the majority states, while the lower panel is relative to the minority states. The value $E - E_F = 0$ corresponds to the Fermi energy. (d) DOS of n-doped graphene (shown is the contribution of the carbon atoms) in the Ho/Gr system (red) and DOS of bare graphene (grey). All calculations where performed including SOC self-consistently.

energy for a hexagonal system reads [48]

$$E_{\text{an}} = K_1 \sin^2\theta + K_2 \sin^4\theta + K_3 \sin^6\theta + K_4 \sin^6\theta \cos 6\varphi. \quad (2)$$

K_i are the magnetic anisotropy constants, θ is the polar angle between the magnetization and z axis, while φ is the azimuthal angle between the magnetization and the x axis. In the following, we compute the anisotropy constants K_i by fitting the changes in the total energy upon rotation of the magnetic moment relative to the crystal lattice. The results are given in Fig. 3 and are obtained self-consistently with DFT + U and SOC as discussed in Sec. II. The dotted data represent the *ab initio* results which are then fitted with the continuous lines using Eq. (2).

Figure 3(a) displays the total energy change within the (xz) plane by steps of 10°. An alternative visualization of the out-of-plane curves in terms of a polar plot is given in panel (b). Figure 3(c) displays the basal anisotropy within the graphene plane with an azimuthal rotation angle φ away from the x axis. The fitted values of K_i are summarized in Table III for the investigated systems. The lowest order constants are an order of magnitude bigger than the third one. The in-plane constants K_4 are again one order of magnitude weaker than K_3 with the exception of Tm. In all three systems, the magnetic anisotropy energy is dominated by the K_1 and K_2 constants and deviates from $\sin^2\theta$, indicating the crucial role of higher order anisotropies in an open $4f$ shell.

The green curve in Fig. 3 shows the anisotropy energy for Dy/Gr, for which an in-plane easy axis is obtained ($\theta = 90°$, $\varphi = 0°$). The energy difference between the easy and the z axis is $\Delta E \simeq 2$ meV, while the energy barrier to overcome to switch the magnetization is about 5.3 meV. Ho/Gr (blue curve) has an intermediate easy axis with the configuration ($\theta = 42.67°$, $\varphi = 30°$), indicating a canted magnetization with respect to the graphene sheet. The positive sign of K_4 leads to a nonzero basal angle $\varphi = 30°$ for the minimal energy.

In Tm/Gr (red curve), the magnetic anisotropy curve is qualitatively similar to Ho/Gr with lower energy barriers and the ground state corresponds to a tilted magnetic configuration ($\theta = 39.08°$, $\varphi = 0°$). The direction of the easy axis for each system can be explained by examining the values K_i. The overall shape of the energy curves can be derived by calculating the second derivative of Eq. (2), neglecting K_3 and K_4 and considering $\sin^2\theta = -K_1/2K_2$, which leads to $\frac{\partial^2 E_{an}}{\partial\theta^2} = -2K_1(\frac{2K_2+K_1}{K_2})$. For all the R/Gr systems, the term in parenthesis is positive and thus the behavior is fully determined by K_1, giving rise to an energy valley if $K_1 < 0$ or an energy hill if $K_1 > 0$. Computing $\frac{\partial^2 E_{an}}{\partial\theta^2}$ for $\theta = 0°, 90°$ permits us to determine the behavior at the extrema. For systems with $K_1 > 0$, such as Dy/Gr, the curve at $\theta = 0$ exhibits a convex trend, whereas for Ho/Gr and Tm/Gr, with $K_1 < 0$, the curve shows a concave shape. Similarly, the curvature at $\theta = 90°$ is governed by $\frac{\partial^2 E_{an}}{\partial\theta^2}|_{\theta=90°} = -2K_1 - 4K_2$, producing a concave

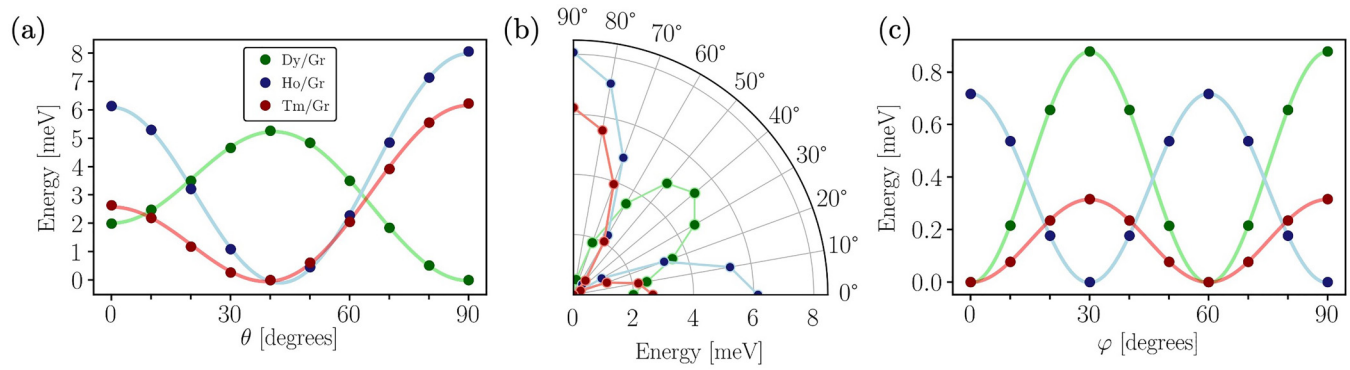

FIG. 3. (a) Out-of-plane $\theta = 0°$ to in-plane $\theta = 90°$ magnetic anisotropy energy curves for Dy (green), Ho (blue), and Tm (red) on graphene: the total energy is plotted as function of the polar angle. (b) Alternative representation of the DFT + U data in a polar plot for the computed systems. (c) In-plane magnetic anisotropy energy curves for Dy, Ho, and Tm on graphene: the total energy is plotted as function of the azimuthal angle φ. Full dots indicate the DFT + U data, while the full lines display the fitting curves.

trend for Ho/Gr and Tm/Gr and a convex shape for Dy/Gr. The in-plane curves in Fig. 3(c) reflect the in-plane sixfold (C_{6v}) symmetry. The functional form of the energy is therefore $\propto \cos 6\varphi$. The amplitude of the oscillation is highest for Dy, followed by Ho and Tm in accordance with the values of K_4 given in Table III.

Nevertheless, the classical formulation described above does not take into account effects at the quantum level that favor magnetization reversal, thus we proceed with a quantum-mechanical description. The CF indeed splits the $(2J + 1)$-fold degeneracy of an isolated atom into sublevels [8]. For the adatoms, the actual form of the CF Hamiltonian depends on the specific point group of the adsorption site. Focusing on the H site of graphene which has a C_{6v} symmetry, the CF Hamiltonian reads [49,50]

$$\hat{H}_{\mathrm{CF}} = C_2^0\hat{O}_2^0 + C_4^0\hat{O}_4^0 + C_6^0\hat{O}_6^0 + C_6^6\hat{O}_6^6, \tag{3}$$

where C_l^m are the CFP, and the $\hat{O}_l^m$ are the Stevens operators [8,47] given in Appendix A. l and m represent the angular and magnetic quantum numbers, respectively, which arise from the formulation of the CF potential in terms of spherical harmonics. These spherical harmonics are then converted in Stevens operators adopting the Stevens operator-equivalent method [51]. The operators of Eq. (3) act on the atomic J_z eigenstates, removing their degeneracy and mixing the different magnetic states. The first three terms contain powers of J and J_z which split the J_z states generating a specific energy landscape of the quantum levels depending on the CFP magnitude and determine the difference between the highest and lowest states, i.e., the energy barrier to overcome to reverse the magnetization. The last term in Eq. (3) contains the ladder operators $\hat{J}_\pm = \hat{J}_x \pm i\hat{J}_y$ in the form $\hat{O}_6^6 = 1/2(\hat{J}_+^6 + \hat{J}_-^6)$, which mixes the J_z states differing by $\Delta J_z = \pm 6, \pm 12$, and can thus possibly generate tunnel-split doublets (symmetric and antisymmetric linear combinations) with quenched $\langle J_z\rangle$ value that can significantly reduce the energy barrier for a spin-flip event inducing quantum tunneling of magnetization. Indeed, when quantum states at $\langle J_z\rangle = 0$ are formed, the system does not necessarily need to overcome the whole energy barrier extending from the ground state to the highest lying state to exhibit magnetization reversal, but can tunnel through this barrier towards the opposite magnetization state, for example, via thermal excitation. In this picture, the CFPs determine how the $\hat{O}_l^m$ split the J_z states and are thus an essential ingredient to understand the mechanisms which determine the magnetic stability of single-atom magnets. Therefore, the knowledge of the CFP is highly demanded and helps identify possible systems protected from magnetization-reversal events that could be an appealing choice for stable magnetic units.

TABLE III. Magnetic anisotropy constants obtained via fitting of DFT + U data depicted in Fig. 3 for Dy, Ho, and Tm on graphene. Units are in meV.

R/Gr	K_1	K_2	K_3	K_4
Dy/Gr	15.355	−18.918	1.536	−0.441
Ho/Gr	−27.734	32.218	−2.591	0.360
Tm/Gr	−13.285	16.720	0.146	−0.158

In the following, we proceed by providing a simple approach to evaluate the CFP: Using first-order perturbation theory, we compute the classical CF energy [52]. Assuming that the magnetic anisotropy energy (MAE) contributions come fully from the 4f orbitals, we then extract the CF coefficients as linear combinations of the K_i constants obtained from the above-discussed fitting. In the limit where the CF effects are small in comparison to the magnetic exchange field, one can focus on the CF contribution to the atomic Hamiltonian and apply first-order perturbation theory. The energy change E_{CF} attributed to $\hat{H}_{\mathrm{CF}}$ then reads [53]

$$\begin{aligned} E_{\mathrm{CF}} &= \sum_{l=2,4,6} C_l^0\langle\hat{O}_l^0\rangle + C_6^6\langle\hat{O}_6^6\rangle, \\ \langle\hat{O}_l^m\rangle &= \langle J, M|\hat{O}_l^m|J, M\rangle \\ &= f_l(J)F_l^m(\theta)G_m(\varphi). \end{aligned} \tag{4}$$

$M = +J$ for heavy R's and $f_l = 2^{-l}(2J)!/(2J - l)!$. The angular functions $F_l^m(\theta)$ and $G_m(\theta)$ are determined in Ref. [53] and listed in Appendix B. By equating Eqs. (2) and (4), we ob-

TABLE IV. Crystal field coefficients obtained via Eq. (5) for Dy, Ho, and Tm on graphene. Results are shown in meV.

	C_2^0	C_4^0	C_6^0	C_6^6
Dy/Gr	0.025	-1.717×10^{-4}	-7.381×10^{-8}	-4.895×10^{-6}
Ho/Gr	−0.039	3.904×10^{-4}	1.992×10^{-7}	6.394×10^{-6}
Tm/Gr	−0.190	9.229×10^{-3}	-8.026×10^{-6}	-2.006×10^{-3}

tain a linear relation between the CFP and the K_i coefficients of the MAE:

$$\begin{aligned} K_1 &= -3f_2C_2^0 - 40f_4C_4^0 - 168f_6C_6^0, \\ K_2 &= 35f_4C_4^0 + 378f_6C_6^0, \\ K_3 &= -231f_6C_6^0, \\ K_4 &= f_6C_6^6. \end{aligned} \tag{5}$$

Using the coefficients K_i and Eq. (5), the CFP can be determined for the ground-state configurations for Dy ($J = 8$), Ho ($J = 15/2$), and for Tm ($J = 7/2$). The results are summarized in Table IV. The sign of C_2^0 determines the orientation of the parabolic dispersion around $J_z = 0$ since it multiplies $\hat{O}_2^0 = 3\hat{J}_z^2 - J(J+1)$, thus it determines the easy axis of the system considering a first-order anisotropy, i.e., when only K_1 is nonzero. A negative C_2^0 corresponds then to an out-of-plane easy-axis ($K_1 > 0$), while a positive C_2^0 is associated to an in-plane easy-axis ($K_1 < 0$).

Considering Dy/Gr with integer $J = 8$, we find the C_2^0 coefficient is positive, leading to a single ground state with $\langle J_z\rangle = 0$, as evidenced in the multiplet splitting shown in Fig. 4. Here, states with the same color represent a mixture of different states differing by $\Delta J_z = \pm6, \pm12$, and therefore can slightly deviate from the expectation values $\langle J_z\rangle$ of pure states. The strength of this mixing is dictated by the value of the C_6^6 parameter. In particular, for Dy/Gr, several of these linear combinations form and of these two sets—one being a mixture of $|J_z = -3\rangle$ and $|J_z = +3\rangle$ (shown in red) and one of $|J_z = -6\rangle$, $|J_z = 0\rangle$, $|J_z = +6\rangle$ (orange, the state at ∼8 meV corresponds to a doublet, better resolved in the inset of Fig. 4)—appear at quenched $\langle J_z\rangle = 0$ value. These kinds of states, in general, can compromise the stability of the magnetization inducing quantum tunneling of magnetization. Nevertheless, in the present case there is a single energy minimum and magnetization reversal is not possible.

We compare the values for Dy/Gr with Ref. [30], where the CFPs are reported in the standard notation $A_l^m\langle r^l\rangle = C_l^m/\theta_l(J)$, with $\theta_l(J)$ the Stevens factors for a total angular momentum J. For the Dy with the configuration $J = 8$ (for Dy^{2+}), the Stevens factors are $(\theta_2, \theta_4, \theta_6) = (-0.222\times10^{-2}, -0.333\times10^{-4}, -1.3\times10^{-6})$ (these are the values associated with Ho^{3+}). The resulting values are $(A_2^0, A_4^0, A_6^0, A_6^6) = (-11.287, 5.156, 0.057, 3.765)$ meV. The largest coefficients, namely, A_2^0 and A_4^0, are in good agreement with the values obtained in Ref. [30] using the Hubbard-I approximation, while deviations in magnitude are observed in A_6^0 and A_6^6. These different values might be a consequence of the supporting Ir substrate included in Ref. [30]. The energy required to overcome the energy barrier from the lowest- to the highest-lying J_z state in the quantum picture is associated to the classical first-order magnetic anisotropy, i.e., the energy involved in the magnetization reversal from out-of-plane to in-plane. Comparing the quantum and classical models, it can be seen that the quantum approach corresponds qualitatively to the classical magnetization rotation, with a in-plane magnetic ground state for Dy/Gr.

Concerning Ho/Gr and Tm/Gr systems, the CFP lead to a degenerate ground state with nonminimal $\langle J_z\rangle$ [Figs. 10(a) and 10(b) in Appendix E, respectively]. The energy trend favors a canted magnetic ground state as determined in the MAE curves. Both magnetic atoms are characterized by a half-integer J value and are protected against the formation of states at $\langle J_z\rangle = 0$ by Kramers degeneracy and, consequently, against quantum tunneling of magnetization via those states, such that, in principle, the system has to overcome the whole energy barrier from the lowest multiplet to the highest-lying multiplet to exhibit spin flip. Nonetheless, based on the values of the higher order CF coefficients, the dispersion of the J_z states can have different nonmonotonic shapes in which a faster way for a spin-flip event might be favored, for example, first-order transitions at finite temperature via phonon or

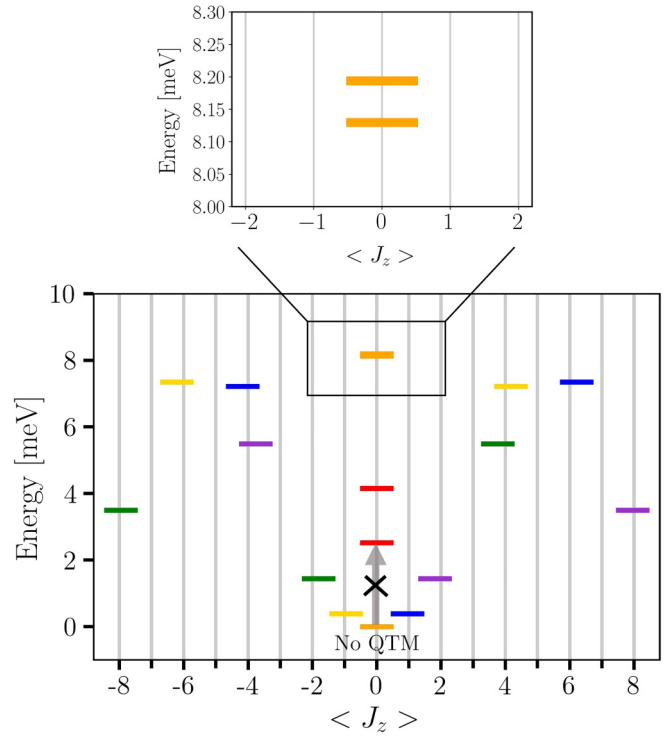

FIG. 4. Multiplet splitting of Dy/Gr adopting the CFP values obtained from reverse engineering via the magnetic anisotropy constants. States in the same color correspond to linear combinations of $|J_z\rangle$ differing by $\Delta J_z = \pm6, \pm12$. Inset shows the ∼50 μeV energy splitting of the $|J_z = -6\rangle$, $|J_z = 0\rangle$, $|J_z = +6\rangle$ doublet

electron scattering events, that can be followed by quantum tunneling of magnetization.

IV. TEMPERATURE EFFECTS

In this section, we discuss the effect of temperature on magnetization reversal or stability. We distinguish two mechanisms in two different temperature regimes. At finite temperatures, magnetization reversal can occur through thermal activation, enabling the system to overcome the minimal energy barrier when the temperature is sufficiently high. This leads to an Arrhenius-like relationship for the magnetic lifetime under the condition that no external magnetic field is present. At lower temperatures, although the thermal energy may not be sufficient to overcome the energy barrier, it can prompt excitations to metastable higher-energy states that enable thermally assisted quantum tunneling of the magnetization [54]. This phenomenon involves scattering processes, such as interactions with substrate phonons. The mathematical representation employs operators $\hat{J}_z$, $\hat{J}_+$, and $\hat{J}_-$, enabling transitions between states characterized by angular momentum changes of $\Delta J_z = 0, \pm 1$. Hence, in this first-order perturbation scenario, the operator $\hat{O}_6^6$ facilitates the coupling between states of equal energy having angular momentum differences of $\Delta J_z = 0 \pm 6k, -1 \pm 6k, 1 \pm 6k$. Here, the parameter k assumes integer values depending on J [20]. This process thus involves the transition to a higher-energy state, from which subsequent quantum tunneling can take place.

Within the scope of the systems under investigation, the Dy/Gr system does not display a magnetic bistability. Instead, it maintains a singular nondegenerate ground state at $\langle J_z \rangle = 0$, consequently ruling out the possibility of magnetization reversal. However, when considering the half-integer spin system Ho/Gr, the two degenerate ground states manifest at $\langle J_z \rangle = \pm 11/2$. The energy barrier separating these two ground states is substantial, approximately $\sim$14 meV, which corresponds to an activation barrier of $U = 162$ K in the expression for the relaxation time $\tau \propto e^{U/k_B T}$, where k_B is the Boltzmann constant and T the temperature. However, interactions with substrate phonons can establish a connection between these two states and the closest accessible states via thermal excitation. Specifically, these accessible states are characterized by $\langle J_z \rangle = \pm 13/2$ and are positioned at an energy gap of roughly $\Delta E \sim 1.8$ meV (21 K), from which assisted quantum tunneling is possible. Shifting focus to the Tm/Gr system, the doubly degenerate ground states possess an expectation value of $\langle J_z \rangle \sim \pm 5/2$. Overcoming the entire energy barrier separating these ground states would require an energy of 209 K (equivalent to 18 meV). Furthermore, there exists an energy gap of 95 K (approximately $\sim$8.2 meV) to the first excited state at $\langle J_z \rangle = \pm 3/2$, which is inherently protected against quantum tunneling. Although the exact determination of life times goes far beyond this paper, from these arguments we conclude that among the two systems studied with out-of-plane anisotropy, Tm/Gr is probably the most stable with respect to magnetization reversal.

V. MAGNETOELASTIC COUPLING

The particularly large MAE found in these materials is a consequence of the localized and partially filled $4f$ shells together with the surrounding CF of the graphene substrate. In the case of a half-filled $4f$ shell with a vanishing total orbital moment $\mathbf{L}$ (Eu and Gd), the SOC contribution of the $4f$ electrons is tiny and hence the MAE is drastically reduced [55,56]. The different values of $\mathbf{L}$ correspond to specific shapes of the charge cloud [57,58] (see Fig. 8) that interact with the neighboring sites as the spin moment $\mathbf{S}$ rotates. Given the strong dependence of the MAE on the shape of $4f$-charge distribution, strong changes in the MAE can occur due to mechanical deformations. The induced strain might, for instance, induce a displacement of the charge density inside the structure and through SOC effect lead to a change in the orientation of $\mathbf{S}$. Here, we simulate the effect of strain on the MAE by changing the height of the R atoms with respect to the graphene sheet and analyze magnetoelastic coupling. From an experimental perspective, this shift in distance can be realized, for instance, by modifying the chemical reactivity or the charge state of the graphene sheet through intercalation of dopands between graphene and the substrate [59–61]. Figures 5(a)–5(c) show the change of the out-of-plane MAE, while Figs. 5(d)–5(f) depict the in-plane MAE. Three different distances were considered, $d/d_0 = \{0.96, 1.0, 1.04\}$, where $d/d_0 = 1.0$ represents the initial relaxed position of the adatom, d being the shifted height, and d_0 the equilibrium height. The MAE is once more obtained from total energy self-consistent calculations (dotted data) and fitted with Eq. (2) (continuous line).

First, we focus on the out-of-plane MAE which increases, in terms of modulus of the K_i constants, as the adatom is compressed towards the surface for all cases. The dependence of the MAE constants K_i as a function of the distance is shown in Figs. 5(g)–5(i), where the systematic increase of the K_i is due to the enhancement of the CF as the impurity gets closer to the substrate. We also note that the complex shapes once more require more coefficients, K_2 and K_3, which result in canted minimum energy solutions for Ho and Tm. As also discussed in Sec. III, the sign of K_1 is reflected in the generation of an energy hill or valley in the MAE curve, which are more pronounced for higher absolute values of K_1. In general, K_2 exhibits an opposite sign when comparing Dy/Gr to Ho and Tm/Gr and a slightly bigger absolute value than K_1 for all the systems. The contribution of K_2 leads to a tilted easy (hard) axis for Ho, Tm (Dy). Also, K_3 exhibits an opposite sign when comparing Dy/Gr with Ho/Gr and Tm/Gr. Nevertheless, the major difference shows up in the module of this constant, which assumes a higher value in the case of Dy (6.821 meV compared to -3.434 meV and -1.032 meV for Ho/Gr and Tm/Gr, respectively) at $d/d_0 = 0.96$, and hence has larger influence on the MAE curve, causing a change in the easy axis from in plane for $d/d_0 = 1.0$ and $d/d_0 = 1.04$ to out of plane for $d = 0.96$.

The in-plane anisotropies in Figs. 5(d)–5(f) display similar behavior as discussed in Sec. III with a periodicity of $\varphi = 60^\circ$. The amplitudes of the oscillations are given in terms of K_4 and, similarly to the out-of-plane coefficients, it is enhanced by the reducing d/d_0. The only exception appears for Tm/Gr, for which $d/d_0 = 1.04$ seems slightly larger than $d/d_0 = 1.0$. A more detailed analysis for the latter is reported in Appendix C.

Comparing the different R's, Tm/Gr shows the smallest $|K_4|$ value; Ho and Dy instead have the same order of mag-

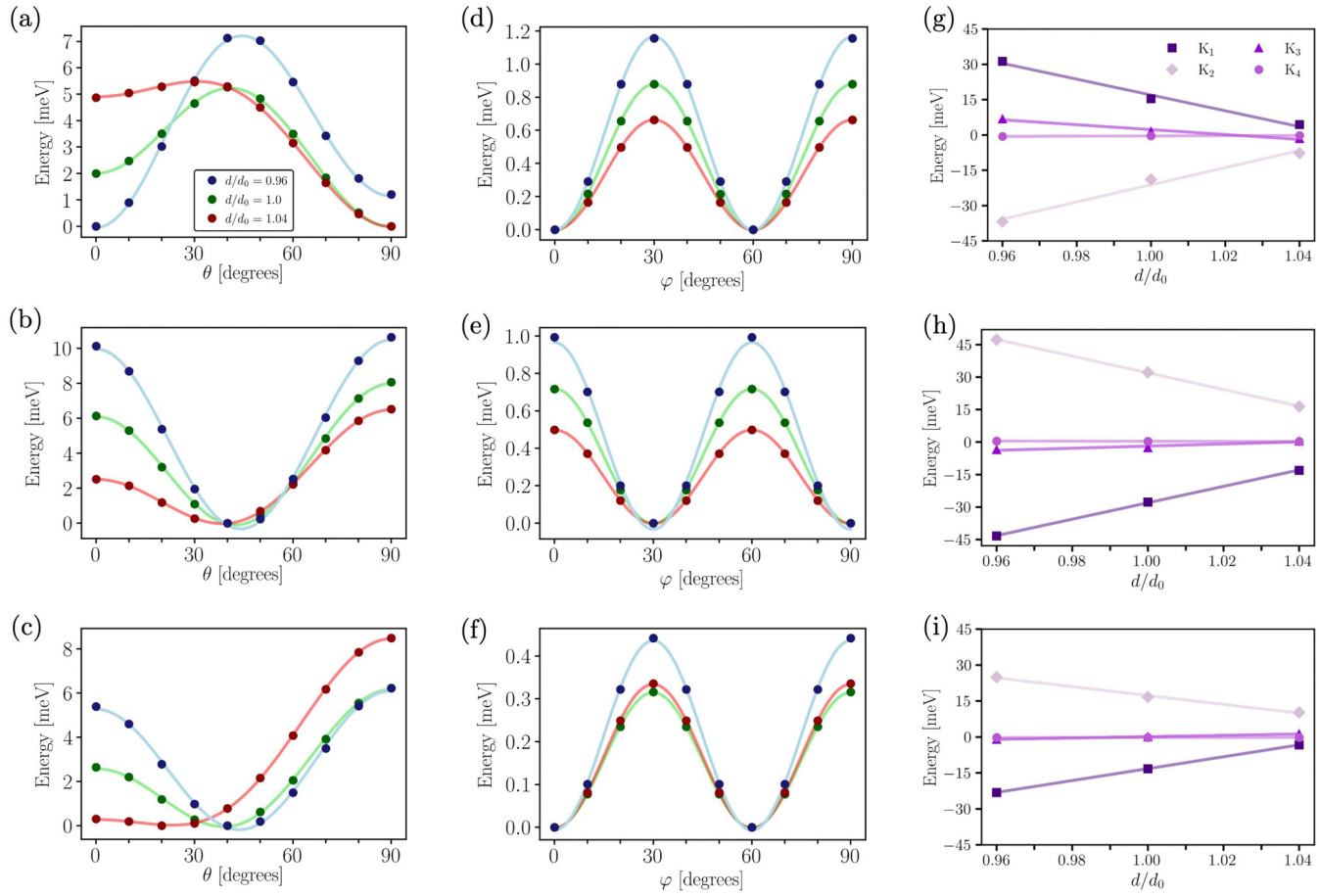

FIG. 5. MAE curves (out-of-plane and in-plane) for different distances, namely, $d/d_0 = 0.96, 1.0, 1.04$ (blue, green, and red, respectively) of the rare-earth adatoms from the graphene monolayer. (a), (d) correspond to the out-of-plane and in-plane curves of Dy/Gr; (b), (e) correspond to the out-of-plane and in-plane curves of Ho/Gr; (c), (f) correspond to the out-of-plane and in-plane curves of Tm/Gr. Note the different scales for the energies of the out-of-plane and in-plane results. For each system, the last column [(g)–(i)] shows the respective magnetic anisotropy constants K_i ($i = 1, 2, 3, 4$) obtained via the fitting of the MAE curves. Specifically, (g) shows the K_i for Dy/Gr, (h) for Ho/Gr, and (i) for Tm/Gr. Points correspond to DFT + U data while lines to the fitting curves.

nitude $K_4 \sim 1$ meV for $d/d_0 = 0.96$, which might reflect a modulation of the charge distribution in the xy plane compared to Tm. Overall, a stronger MAE emerges when the R atom is pressed against the graphene sheet, since the $4f$ and $5d$ electrons of the impurity feel a stronger electrostatic repulsion from the carbon atoms. Figure 6(a) shows the energy difference $\Delta E = E_\parallel - E_\perp$, with $E_\parallel$ being the total energy when the magnetization is aligned along the x axis (parallel to the graphene), while $E_\perp$ represents the total energy with magnetization along the z axis (perpendicular to the graphene), as a function of d/d_0. We scan the values of the MAE for values ranging in $d/d_0 = [0.9, 1.04]$ using a step of 0.01. Positive values of the ΔE indicate that an out-of-plane magnetization is favored compared to an in-plane magnetization.

For Ho/Gr and Tm/Gr, ΔE decreases when the adatom is compressed towards the graphene from $d/d_0 = 1.04$ to smaller distances, going via a minimum and then increasing steeply for high compression of around 10%. In contrast, Dy undergoes a switch of the favored magnetization direction, since in the case of high compression an out-of-plane is more stable, while the in-plane direction appears lower in energy for larger distances from the graphene. Such a mutable magnetic behavior might find interesting applications in engineering magnetomechanical nanodevices that rely on pressure-induced magnetization transitions [62–64].

We show in Fig. 6(b) the evolution of the total energy, reported with respect to the energy minimum (placed at 0 eV), as a function of d/d_0 considering an out-of-plane orientation of the moment for Ho/Gr (we obtain very similar curves for Dy/Tm). The same calculations have also been performed with in-plane magnetization for each system and in total six energy curves have been obtained and fitted adopting a Morse potential. The Morse fit is shown in a continuous line and has been performed using Eq. (D1), given in Appendix D. The fit provides the dissociation energy D_e with respect to the minimum at the equilibrium distance and the width b of the curve. These values are then employed to calculate the force constant k_e at the equilibrium position of the oscillator as $k_e = 2b^2 D_e$, which defines the stiffness against deformation. The vibrational frequency ν of the displacement is evaluated following Eq. (D2). Table V summarizes the results obtained for the R/Gr systems: k_e and ν calculated for the two directions of the magnetization, namely, parallel to the Gr plane ($\parallel$) and perpendicular ($\perp$). There is a slight dependence of

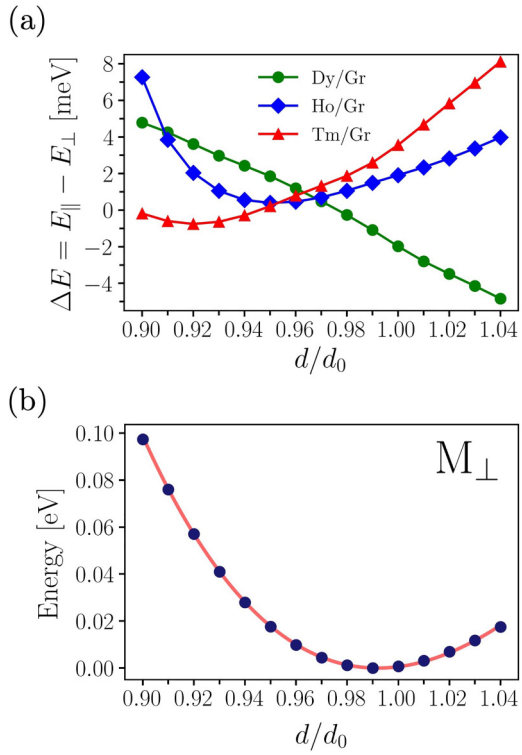

FIG. 6. (a) Magnetic anisotropy energy as a function of the distance of the R with respect to graphene for Dy (green), Ho (blue), and Tm (red) calculated with DFT + U. (b) Total energy as a function of the distance of the Ho adatom from the graphene sheet calculated with DFT + U (full dots) and the respective fit with a Morse-like potential (line).

the vibrational frequencies on the magnetization orientation changes. For Dy, the force constant k_e at equilibrium is bigger for an out-of-plane magnetization, meaning the material is more resistant against deformation when perpendicularly magnetized, which reflects in a slightly higher vibrational frequency of the mode [see Eq. (D2) in Appendix D]. Ho and Tm have a higher k_e and ν for the in-plane magnetization direction. Lastly, among the systems at hand, Tm/Gr displays the lowest k_e values, which determines the weakest bonding towards the substrate and makes it the most malleable 2D material in the set.

Taking into account the bistability observed in the multiplet spectra of Ho/Gr and Tm/Gr (Fig. 10), there exists a separation between the two ground states with energy gaps of approximately $\Delta E \sim 14$ meV and $\Delta E \sim 18$ meV, respectively. When converting the vibrational frequencies of the R atoms' modes into vibrational energies, we obtain values ranging from $h\nu = 60 - 70$ meV. This implies that magnetization reversal due to adatom vibrations, which would necessitate $\Delta E = h\nu$, is unlikely.

TABLE V. Elastic force constants k_e (N/m) and the respective vibration frequencies ν (s^{-1}) calculated with perpendicular and parallel magnetization for each R/Gr system.

R/Gr	$k_{e\perp}$	$k_{e\parallel}$	$\nu_{\perp} \times 10^{-13}$	$\nu_{\parallel} \times 10^{-13}$
Dy/Gr	1155.54	1118.13	1.879	1.848
Ho/Gr	1029.05	1076.14	1.769	1.809
Tm/Gr	784.72	908.63	1.539	1.656

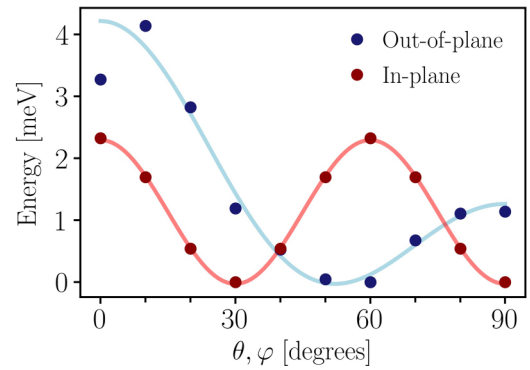

FIG. 7. Out-of-plane (blue) and in-plane (red) magnetic anisotropy energy curves for Dy/Gr with Dy with orbital momentum $m_l^{\mathrm{R}} = 5\ \mu_{\mathrm{B}}$. The blue dots indicate the DFT + U energies, while the line corresponds to the fitting.

VI. DYSPROSIUM ON GRAPHENE: DEVIATION FROM HUND'S RULES

The calculations presented above are based on the occupation of 4f shells following a Hund-like ground state. Nonetheless, further analysis shows that for Dy/Gr, an orbital occupation can be obtained, where one majority spin electron moves from the orbital with quantum number $m_l = 1$ to $m_l = 0$, partially quenching the orbital moment to $m_l^R = 4.9\mu_{\mathrm{B}}$. This indicates that for this particular case of Dy/Gr, the CF effects are strong enough to compete with the Hund's exchange. This re-arrangement affects mainly the orbital moment as it leaves unaltered $m_s^R = 4.03\mu_{\mathrm{B}}$, hence only breaking Hund's second rule (maximizes L) and leading to a total angular momentum $J = 7$. Next, we investigate the behavior of the magnetic anisotropy in this new orbital configuration. We will refer to this 4f occupation as the $J = 7$ state and to the Hund's rules orbital occupation as the $J = 8$ state. Specifically, the energy difference calculated between the two observed magnetic states is 0.28 eV in favor of the $J = 7$ situation.

Given the close link between the orbital moment and the MAE, we expect a deviation from the angular dependence determined for the $J = 8$ state shown in Fig. 3. This distinct angular form is attributed to the new shape of the 4f charge cloud in the $J = 7$ state with respect to the $J = 8$ state as depicted in Fig. 8. Indeed, the angular dependence of the MAE curve is driven by the interplay of the charge cloud's geometry and the CF symmetry: a rotation of the magnetization corresponds to a rotation of the anisotropic charge distribution through SOC interaction and can thus lead to stronger/weaker electrostatic repulsion if the charge cloud lies closer/farther away from the point charges defining the CF. Figure 7 shows the respective out-of-plane and in-plane MAE curves, where the dots (full lines) represent the DFT + U data (fits). The fitted MAE coefficients K_i using Eq. (2) are given in Table VI, the out-of-plane anisotropy has a minimum at a

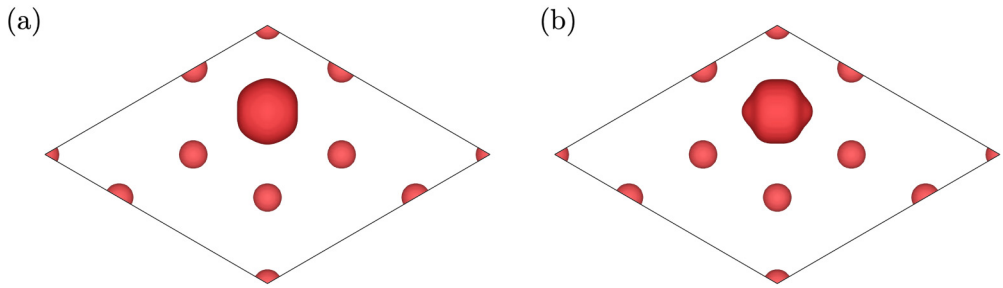

FIG. 8. Total charge density of the R and Gr atoms of the spin-down channel of Dy/Gr with in-plane magnetization for the two different orbital moments: (a) $m_l = 6\ \mu_B$ ($J = 8$), (b) $m_l = 5\ \mu_B$ ($J = 7$). For atom positions, compare with Fig. 1 with the Dy atom in the H site.

canted angle $\theta \simeq 51.82^\circ$, while the basal-anisotropy favors an angle $\varphi = 30^\circ \pm \frac{\pi}{3}$.

For the out-of-plane case, the shape of the MAE curve is drastically different when comparing the $J = 7$ state (Fig. 7) with the $J = 8$ state [Fig. 3(a)]. Here, instead of an energy barrier between the perpendicular magnetization ($\theta = 0^\circ$) and the in-plane magnetization ($\theta = 90^\circ$), there is an energy valley. These trends are reflected in the K_i coefficients, which have opposite signs when comparing the two orbital configurations (see Table VI).

Interestingly, the in-plane MAE shown in red in Fig. 7 is boosted and reaches values of the same order of magnitude as its out-of-plane counterpart. It is the largest in-plane MAE observed for all systems at hand and this enhancement is reflected in the K_4 coefficient which causes a global minima ($\frac{\partial E_{an}}{\partial \theta}|_{\varphi=30^\circ}$) at $(\theta, \varphi) = (57.93^\circ, \varphi = 30^\circ \pm \frac{\pi}{3})$. We note that this energy minimum does not coincide with minimum defined by the purely out-of-plane MAE ($\frac{\partial E_{an}}{\partial \theta}|_{\varphi=0^\circ}$) located at $\theta = 51.82^\circ$. Qualitatively, this large K_4 can be understood due to the shape of the $4f$ charge density in Fig. 8 that shows the spin-down charge density computed for the in-plane magnetization $\parallel x$ axis. Indeed, for the $J = 7$ state there is a larger spin-down density in the xy plane ($\parallel$ to the substrate) in contrast to the $J = 8$ state, for which the charge density displays smaller poles in the xy plane.

These findings demonstrate the necessity of a careful assessment of the $4f$-orbital occupation when dealing with R-based systems in low dimensions. This is also important if one wants to use the above-proposed reverse-engineering method to determine the CFP, since it holds only valid in the context of a Hund's rule occupation, i.e., when the interelectronic repulsion and SOC effects dominate and the CF can be treated as a perturbation. Further advanced methods such as the Hubbard-I approximation [31] will be considered in the future along with a comparison to experimental data.

TABLE VI. Magnetic anisotropy constants K_i for the $J = 7$ and $J = 8$ states in Dy/Gr. Results are in meV.

State	K_1	K_2	K_3	K_4
J=7	−14.29	13.10	−1.76	1.16
J=8	15.36	−18.92	1.54	−0.44

VII. REVISITING THE CHOICE OF SUPERCELL SIZE

Since the magnetic properties of R atoms on graphene or similar substrates primarily arise from the behavior of the highly localized $4f$ electrons, the relatively compact $\sqrt{3} \times \sqrt{3}$ supercell is expected to adequately capture the magnetic anisotropy. As expressed in Sec. II A, the choice of the supercell was motivated by the experimentally observed coverage of Eu on graphene [37,38]. In light of the fact that numerous experiments and theoretical studies [16,20,25,26,30,65] involve more diluted coverage of R atoms, we conducted a comparison of the ground-state properties between a 4×4 supercell and a $\sqrt{3} \times \sqrt{3}$ cell for the R/Gr complexes, both at the same perpendicular distance of the R atom and using the same computatonal parameters. The results, including the d and f occupations, as well as the spin and orbital magnetic moments of the R atoms, are presented in Table VII.

In comparison to the $\sqrt{3} \times \sqrt{3}$ results (Table II), the change in the orbital moment m_l^{R} is minimal, amounting to less than 50 mμ_B, while the spin moment m_s^{R} undergoes a change of approximately 100 mμ_B. The variation of the spin moment is caused by the reduction of hybridization among the delocalized valence $6s$, $6p$, and $5d$ electrons, as a consequence of the larger separation between the R atoms. In this atomic limit, there is a shift in the population of states from $5d$ to $6sp$, leading to a slightly increase in the magnetic moment primarily originating from the spin-polarized $6s$ electrons. This slight enhancement in the spin magnetic moment may have an impact on magnetic anisotropy, but generally, the contribution of valence electrons to the MAE is a small fraction, approximately 10%, of the total interaction energy between the R atom and the CF. Conversely, the magnetic anisotropy can be in first approximation explained as originating from the electrostatic interaction between the nonspherical charge den-

TABLE VII. Ground-state properties of R/Gr in a 4×4 supercell: d and f occupations, spin m_s^R, and orbital m_l^R magnetic moments. Calculations are performed with SOC in presence of a perpendicular spin-quantization axis.

Rare earth	d_{occ}	f_{occ}	m_s^R (μ_B)	m_l^R (μ_B)
Dy	0.181	9.915	4.156	5.916
Ho	0.165	10.913	3.159	5.936
Tm	0.155	12.901	1.163	2.989

sity, primarily determined by the orbital magnetic moment, and the CF of graphene. Given the minor changes observed in the orbital moments, significant deviations in the magnetic anisotropy are not expected.

From another perspective, the electron redistribution within the valence orbitals observed in the 4×4 case can alter the interaction between the R atom with graphene, resulting in a small change in the perpendicular distance between the R atom and graphene. Consequently, this affects the CF generated by Gr and experienced by the R atom. Nonetheless, as illustrated in Figs. 5 and 6(a), it is evident that the magnetic anisotropy (and the respective constants K_i) trend remains approximately linear in the vicinity of $d/d_0 = 1$.

VIII. CONCLUSION

In this paper, we investigated the electronic structure of a selected subset of $4f$ adatoms (Dy, Ho, and Tm) deposited on graphene and treated the localized $4f$ electrons using the DFT + U approach. The R/Gr complexes display a metallic behavior due to n doping originating from the R's d orbitals. In all the analyzed R/Gr systems, the R atoms adopt a divalent configuration R^{2+} in which the orbital occupation of Ho and Tm is consistent with a maximal orbital moment, while Dy displays a lower energy for a $J = 7$ configuration instead of $J = 8$ (Hund's rules). This deviation originates from the competition between the CF and intra-atomic exchange. The f states maintain a localized behavior and carry a high orbital moment which results in a consequently large single-ion magnetic anisotropy. The self-consistent total energy calculations show barriers of several meV upon variation of the magnetization direction.

From the MAE curves, we extracted the magnetic anisotropy constants which are then reverse engineered to CFP in the Stevens convention. The obtained CFP are then adopted in the diagonalization of the CF Hamiltonian matrix in the C_{6v} symmetry to calculate the multiplet structure of each system. Half-integer spin systems (Ho/Gr and Tm/Gr) do not present tunnel-split doublets at $\langle J_z \rangle = 0$ and are thus protected against quantum tunneling of magnetization via such states, while in Dy/Gr in the $J = 8$ state, we find that the high-order CFP C_6^6 generates potential states at quenched $\langle J_z \rangle$ that might reduce the energy barrier for spin reversal. Nevertheless, in the latter case we find a single magnetic ground state at $\langle J_z \rangle = 0$ with no possibility of reversal. Further studies to determine systems with high magnetic anisotropy energies and protection against magnetization reversal might involve the analysis of the effect of the symmetry of different substrates on the multiplet splittings as well as the impact of the chemical composition of the CF, i.e., inducing stronger SOC and/or orbital hybridizations to the adsorbed R atom.

The analysis of the magnetic anisotropy is then further extended to inspect magnetoelastic effects. The application of a perpendicular strain compressing the adatom towards the graphene enhances the magnetic anisotropy, thus providing another mechanism to amplify the magnetic stability of these $4f$ adatoms. Increasing the adatom-substrate distance leads to a decoupling from the substrate, driving the atom to a quasi-isolated state, ultimately reducing the magnetic anisotropy. A deviation from this behavior has been observed for the in-plane anisotropy constant K_4 in the case of Tm/Gr, where a non-monotonous trend is found as a function of the strain. For the particular case of Dy/Gr, the mechanical strain induces a change in the sign of the energy difference $\Delta E = E_\parallel - E_\perp$ in the $J = 8$ magnetic state, indicating the possibility to tailor the favored magnetization direction by application of an external stress.

Although the magnetic anisotropy energies of R atoms are studied using $\sqrt{3} \times \sqrt{3}$ supercells, we expect small quantitative but no significant qualitative changes for the anisotropy energies of individual R atoms calculated in larger supercells. For higher R atom densities, as simulated in a 1×1 unit cell, we expect both larger quantitative and qualitative differences.

Finally, our first-principles investigation emphasizes the necessity of a detailed analysis of the orbital occupations within these $4f$ systems, as it can lead to qualitatively and quantitatively different magnetic anisotropies.

ACKNOWLEDGMENTS

J.P.C. acknowledges Dr. E. Mendive Tapia for inspiring discussions concerning magnetoelastic phenomena; and H. Janßen for advice on FLEUR calculations. The project is funded by the Deutsche Forschungsgemeinschaft (DFG) through CRC 1238, Control and Dynamics of Quantum Materials: Spin orbit coupling, correlations, and topology (Project No. 277146847 C01). This research is also supported by the FLAG-ERA grant SOgraphMEM, Project No. PCI2019-111867-2. We acknowledge computing resources granted by RWTH Aachen University under Project No. jara0219.

APPENDIX A

The Stevens operators $\hat{O}_l^m$ for a C_{6v} CF read

$$\begin{aligned}
\hat{O}_2^0 &= 3\hat{J}_z^2 - X, \\
\hat{O}_4^0 &= 35\hat{J}_z^4 - (30X - 25)\hat{J}_z^2 + 3X^2 - 6X, \\
\hat{O}_6^0 &= 231\hat{J}_z^6 - (315X - 735)\hat{J}_z^4 \\
&\quad + (105X^2 - 525X + 294)\hat{J}_z^2 \\
&\quad - 5X^3 + 40X^2 - 60X, \\
\hat{O}_6^6 &= \tfrac{1}{2}[\hat{J}_+^6 + \hat{J}_-^6],
\end{aligned} \tag{A1}$$

where $X = J(J+1)$, $\hat{J}_+ = \hat{J}_x + i\hat{J}_y$, $\hat{J}_- = \hat{J}_x - i\hat{J}_y$. The selection rules for nonzero elements of the lm expansion are dictated by the lattice symmetry. For the $4f$ shell in C_{6v} symmetry, the expansion of $\hat{H}_{\mathrm{CF}}$ is defined by the quantum numbers $l = \{0, 2, 4, 6\}$ and $m = 0, 6$.

APPENDIX B

In the following, the angular functions appearing in Eq. (4) are defined:

$$\begin{aligned}
F_2^0(\theta) &= -3\sin^2\theta, \\
F_4^0(\theta) &= 35\sin^4\theta - 40\sin^2\theta, \\
F_6^0(\theta) &= -231\sin^6\theta + 378\sin^4\theta - 168\sin^2\theta, \\
F_6^6(\theta) &= \sin^6\theta,
\end{aligned}$$

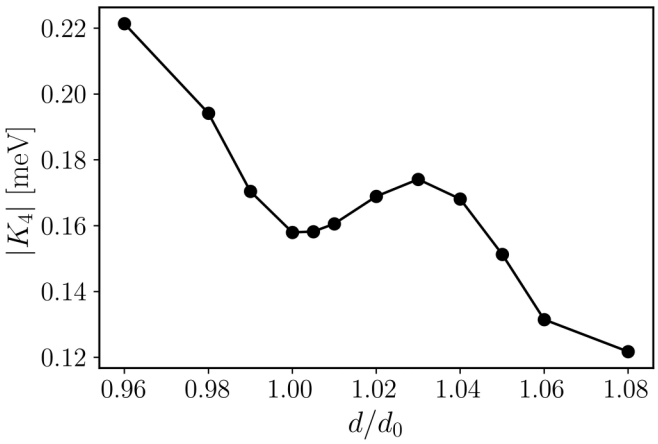

FIG. 9. $|K_4|$ of Tm/Gr for distances ranging from $d = 0.96$ to $d = 1.08$ from the graphene sheet, i.e., from -4% to $+8\%$ of perpendicular strain.

$$G_0(\varphi) = 1,$$
$$G_6(\varphi) = \cos\varphi. \tag{B1}$$

The F_l^m functions define pure out-of-plane rotation and the G_m functions are related to in-plane rotations.

APPENDIX C

In Fig. 9, the modulus of the magnetic anisotropy constant K_4 for Tm/Gr is plotted against different perpendicular strains d/d_0 from the graphene monolayer. Overall, the modulus $|K_4|$ displays a nonlinear behavior first increasing from $d/d_0 = 1.08$ until a maximum is reached at $d/d_0 = 1.03$, then the module shows a decreasing trend until $d/d_0 = 1.0$, after which $|K_4|$ grows again for small distances.

APPENDIX D

The potential energy function adopted in the fitting of the data in Fig. 6(b) of Sec. V reads [66,67]

$$V(r) = D_e(1 - e^{-b(d-d_0)})^2, \tag{D1}$$

where D_e corresponds to the depth of the potential with respect to the dissociation energy, d is the distance between R and Gr, and d_0 is the equilibrium distance. b determines the width of the potential well. The frequency of the vibrational modes in the R/Gr complexes is evaluated as in a diatomiclike system,

$$\nu = \frac{1}{2\pi}\sqrt{\frac{k_e}{\mu}}, \tag{D2}$$

k_e being the force constant of the R-Gr interaction and μ the reduced mass $\mu = \frac{m_{\rm Gr} m_R}{m_{\rm Gr}+m_R}$ of the R/Gr complex, with $m_{\rm R}$ the atomic mass of the R atom and $m_{\rm Gr}$ the mass of graphene in the considered simulation cell involving six carbon atoms, equal to 72.066 amu.

TABLE VIII. Character table of the C_{6v} symmetry group and of the rotational invariant Tm atom with total angular momentum $J = \frac{7}{2}$.

C_{6v}	E	$\bar{E}$	C_2 $\bar{C}_2$	$2C_3$	$2\bar{C}_3$	$2C_6$	$2\bar{C}_6$	$3\sigma_d$ $3\bar{\sigma}_d$	$3\sigma_v$ $3\bar{\sigma}_v$
Γ_1	1	1	1	1	1	1	1	1	1
Γ_2	1	1	1	1	1	1	1	−1	−1
Γ_3	1	1	−1	1	1	−1	−1	1	−1
Γ_4	1	1	−1	1	1	−1	−1	1	1
Γ_5	2	2	−2	−1	−1	1	1	0	0
Γ_6	2	2	2	−1	−1	−1	−1	0	0
Γ_7	2	−2	0	1	−1	$\sqrt{3}$	$-\sqrt{3}$	0	0
Γ_8	2	−2	0	1	−1	$-\sqrt{3}$	$\sqrt{3}$	0	0
Γ_9	2	−2	0	−2	2	0	0	0	0
Tm K_h	8	−8	0	1	−1	$-\sqrt{3}$	$\sqrt{3}$	0	0

APPENDIX E

For the determination of the multiplet structures, we follow the tables in Ref. [47] for the calculation of the matrix elements of the CF Hamiltonian in Eq. (3). In the following, the CF matrix for Tm is provided as an example. From the DFT + U calculations, it is understood that in Tm/Gr the $4f$ electrons closely follow Hund's rules, providing a total angular momentum $J = \frac{7}{2}$, and hence J_z taking values $\{-\frac{7}{2}, -\frac{5}{2}, -\frac{3}{2}, -\frac{1}{2}, \frac{1}{2}, \frac{3}{2}, \frac{5}{2}, \frac{7}{2}\}$. The respective 8×8 CF matrix is given by

$$\begin{pmatrix} A & 0 & 0 & 0 & 0 & 0 & E & 0 \\ 0 & B & 0 & 0 & 0 & 0 & 0 & E \\ 0 & 0 & C & 0 & 0 & 0 & 0 & 0 \\ 0 & 0 & 0 & D & 0 & 0 & 0 & 0 \\ 0 & 0 & 0 & 0 & D & 0 & 0 & 0 \\ 0 & 0 & 0 & 0 & 0 & C & 0 & 0 \\ E & 0 & 0 & 0 & 0 & 0 & B & 0 \\ 0 & E & 0 & 0 & 0 & 0 & 0 & A \end{pmatrix} \tag{E1}$$

and the matrix elements $\langle J_z = i|\hat{H}_{\rm CF}|J_z = j\rangle$ are defined as

$$\begin{aligned} A &= \langle \tfrac{7}{2}|\hat{H}_{\rm CF}|\tfrac{7}{2}\rangle = \langle -\tfrac{7}{2}|\hat{H}_{\rm CF}|-\tfrac{7}{2}\rangle \\ &= 21C_2^0 + 420C_4^0 + 1260C_6^0, \\ B &= \langle \tfrac{5}{2}|\hat{H}_{\rm CF}|\tfrac{5}{2}\rangle = \langle -\tfrac{5}{2}|\hat{H}_{\rm CF}|-\tfrac{5}{2}\rangle \\ &= 3C_2^0 - 780C_4^0 - 6300C_6^0, \\ C &= \langle \tfrac{3}{2}|\hat{H}_{\rm CF}|\tfrac{3}{2}\rangle = \langle -\tfrac{3}{2}|\hat{H}_{\rm CF}|-\tfrac{3}{2}\rangle \\ &= -9C_2^0 - 180C_4^0 + 11340C_6^0, \\ D &= \langle \tfrac{1}{2}|\hat{H}_{\rm CF}|\tfrac{1}{2}\rangle = \langle -\tfrac{1}{2}|\hat{H}_{\rm CF}|-\tfrac{1}{2}\rangle \\ &= -15C_2^0 + 540C_4^0 - 6300C_6^0, \\ E &= \langle \tfrac{7}{2}|\hat{H}_{\rm CF}|-\tfrac{5}{2}\rangle = \langle -\tfrac{7}{2}|\hat{H}_{\rm CF}|\tfrac{5}{2}\rangle = \langle \tfrac{5}{2}|\hat{H}_{\rm CF}|-\tfrac{7}{2}\rangle \\ &= \langle -\tfrac{5}{2}|\hat{H}_{\rm CF}|\tfrac{7}{2}\rangle = 360\sqrt{7}C_6^6, \end{aligned} \tag{E2}$$

where the C_l^m are the CF parameters. The exact values in front of each CFP correspond to the matrix element of the respective Stevens operator between the same states ($i = j$) for the diagonal terms, for example, $\langle \frac{7}{2}|\hat{O}_2^0|\frac{7}{2}\rangle = 21$, while

the only nonzero terms of $\langle J_z = i|\hat{O}_6^6|J_z = j\rangle$ with $i \neq j$ are those between J_z states differing by 6. Hence, the matrix is symmetric and presents nonzero off-diagonal terms for the J_z state differing by $\Delta J_z = \pm 6$, which are mixed by the C_6^6 operator. The CF matrix is set up by inserting the C_l^m values obtained via DFT + U calculations and diagonalized, leading to eight eigenvectors in the case of Tm. Concerning the degeneracy of the states, it can be worked out following the orthogonality theorem to determine how the energy levels of an isolated spherically symmetric (K_h) Tm atom split into a sum of irreducible representations (IRs) of the C_{6v} point group:

$$\sum_{\nu=1}^{n} \chi^{(\alpha)}(g_\nu)[\chi^{(\beta)}(g_\nu)]^* = n\delta_{\alpha\beta}. \tag{E3}$$

Here, $\chi^{(\alpha)}$ and $\chi^{(\beta)}$ are the characters of the two compared representations α and β, and the index ν sums over the number n of symmetry operations, which is $n = 24$ for the C_{6v} case. The character table of the two space groups is shown in Table VIII.

To obtain the splitting, one multiplies the character of each operation of the K_h group with the respective character of the C_{6v} group and sums this value over all symmetry operations for each IR in the C_{6v} group separately. The characters are orthogonal, which means that either this sum gives 0 and thus the respective IR of the C_{6v} group is not included or the sum is an integer, n, which tells us how many times the IR is included. In the case of Tm/Gr, Eq. (E3) gives rise to a splitting of four sets of double degenerate state, two sets of which belong to the same IR, namely, Γ_8:

$$K_h^{7/2} = \Gamma_7 + 2\Gamma_8 + \Gamma_9. \tag{E4}$$

The multiplets for Tm/Gr and Ho/Gr are shown in Fig. 10.

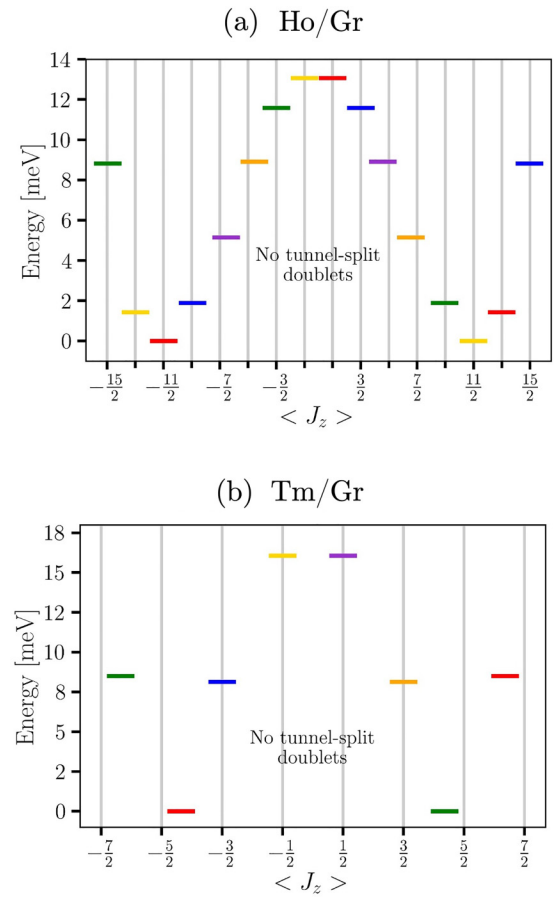

FIG. 10. Multiplet splitting of (a) Ho/Gr and (b) Tm/Gr adopting the CFP values obtained from reverse engineering via the magnetic anisotropy constants. States in the same color correspond to linear combinations of $|J_z\rangle$ differing by $\Delta J_z = \pm 6, \pm 12$.

[1] H.-W. Guo, Z. Hu, Z.-B. Liu, and J.-G. Tian, Stacking of 2D materials, Adv. Funct. Mater. **31**, 2007810 (2021).

[2] P. Miró, M. Audiffred, and T. Heine, An atlas of two-dimensional materials, Chem. Soc. Rev. **43**, 6537 (2014).

[3] S. Manzeli, D. Ovchinnikov, D. Pasquier, O. V. Yazyev, and A. Kis, 2D transition metal dichalcogenides, Nat. Rev. Mater. **2**, 17033 (2017).

[4] K. Novoselov, A. Mishchenko, A. Carvalho, and A. Castro Neto, 2D materials and van der Waals heterostructures, Science **353**, aac9439 (2016).

[5] Y. Liu, N. O. Weiss, X. Duan, H.-C. Cheng, Y. Huang, and X. Duan, van der Waals heterostructures and devices, Nat. Rev. Mater. **1**, 1 (2016).

[6] A. K. Geim and I. V. Grigorieva, van der Waals heterostructures, Nature (London) **499**, 419 (2013).

[7] E. C. Ahn, 2D materials for spintronic devices, npj 2D Mater. Appl. **4**, 17 (2020).

[8] J. Jensen and A. R. Mackintosh, *Rare-Earth Magnetism* (Clarendon Press Oxford, 1991).

[9] T. Schuh, T. Miyamachi, S. Gerstl, M. Geilhufe, M. Hoffmann, S. Ostanin, W. Hergert, A. Ernst, and W. Wulfhekel, Magnetic excitations of rare earth atoms and clusters on metallic surfaces, Nano Lett. **12**, 4805 (2012).

[10] J. Ibañez-Azpiroz, M. dos Santos Dias, S. Blügel, and S. Lounis, Zero-point spin-fluctuations of single adatoms, Nano Lett. **16**, 4305 (2016).

[11] J. Bouaziz, J. Ibanez-Azpiroz, F. S. M. Guimarães, and S. Lounis, Zero-point magnetic exchange interactions, Phys. Rev. Res. **2**, 043357 (2020).

[12] M. Grimm, A. Beckert, G. Aeppli, and M. Müller, Universal quantum computing using electronuclear wavefunctions of rare-earth ions, PRX Quantum **2**, 010312 (2021).

[13] S. Bertaina, S. Gambarelli, A. Tkachuk, I. Kurkin, B. Malkin, A. Stepanov, and B. Barbara, Rare-earth solid-state qubits, Nat. Nanotechnol. **2**, 39 (2007).

[14] F. Huttmann, D. Klar, N. Atodiresei, C. Schmitz-Antoniak, A. Smekhova, A. J. Martínez-Galera, V. Caciuc, G. Bihlmayer, S. Blügel, T. Michely *et al.*, Magnetism in a graphene-4f − 3d hybrid system, Phys. Rev. B **95**, 075427 (2017).

[15] M. Pivetta, F. Patthey, I. Di Marco, A. Subramonian, O. Eriksson, S. Rusponi, and H. Brune, Measuring the

intra-atomic exchange energy in rare-earth adatoms, Phys. Rev. X **10**, 031054 (2020).

[16] X. Liu, C. Z. Wang, M. Hupalo, Y. X. Yao, M. C. Tringides, W. C. Lu, and K. M. Ho, Adsorption and growth morphology of rare-earth metals on graphene studied by *ab initio* calculations and scanning tunneling microscopy, Phys. Rev. B **82**, 245408 (2010).

[17] C. Nistor, A. Mugarza, S. Stepanow, P. Gambardella, K. Kummer, J. L. Diez-Ferrer, D. Coffey, C. de la Fuente, M. Ciria, and J. I. Arnaudas, Structure and magnetism of Tm atoms and monolayers on W(110), Phys. Rev. B **90**, 064423 (2014).

[18] V. Bellini, S. Rusponi, J. Kolorenč, S. K. Mahatha, M. A. Valbuena, L. Persichetti, M. Pivetta, B. V. Sorokin, D. Merk, S. Reynaud, D. Sblendorio, S. Stepanow, C. Nistor, P. Gargiani, D. Betto, A. Mugarza, P. Gambardella, H. Brune, C. Carbone, and A. Barla, Slow magnetic relaxation of Dy adatoms with in-plane magnetic anisotropy on a two-dimensional electron gas, ACS Nano **16**, 11182 (2022).

[19] A. Singha, R. Baltic, F. Donati, C. Wäckerlin, J. Dreiser, L. Persichetti, S. Stepanow, P. Gambardella, S. Rusponi, and H. Brune, $4f$ occupancy and magnetism of rare-earth atoms adsorbed on metal substrates, Phys. Rev. B **96**, 224418 (2017).

[20] R. Baltic, F. Donati, A. Singha, C. Wäckerlin, J. Dreiser, B. Delley, M. Pivetta, S. Rusponi, and H. Brune, Magnetic properties of single rare-earth atoms on graphene/Ir(111), Phys. Rev. B **98**, 024412 (2018).

[21] F. Donati, A. Singha, S. Stepanow, C. Wäckerlin, J. Dreiser, P. Gambardella, S. Rusponi, and H. Brune, Magnetism of Ho and Er atoms on close-packed metal surfaces, Phys. Rev. Lett. **113**, 237201 (2014).

[22] F. Donati, M. Pivetta, C. Wolf, A. Singha, C. Wäckerlin, R. Baltic, E. Fernandes, J.-G. de Groot, S. L. Ahmed, L. Persichetti, C. Nistor, J. Dreiser, A. Barla, P. Gambardella, H. Brune, and S. Rusponi, Correlation between electronic configuration and magnetic stability in Dysprosium single atom magnets, Nano Lett. **21**, 8266 (2021).

[23] F. Donati, S. Rusponi, S. Stepanow, C. Wäckerlin, A. Singha, L. Persichetti, R. Baltic, K. Diller, F. Patthey, E. Fernandes, J. Dreiser, Ž. Šljivančanin, K. Kummer, C. Nistor, P. Gambardella, and H. Brune, Magnetic remanence in single atoms, Science **352**, 318 (2016).

[24] M. Pivetta, S. Rusponi, and H. Brune, Direct capture and electrostatic repulsion in the self-assembly of rare-earth atom superlattices on graphene, Phys. Rev. B **98**, 115417 (2018).

[25] R. Baltic, M. Pivetta, F. Donati, C. Wäckerlin, A. Singha, J. Dreiser, S. Rusponi, and H. Brune, Superlattice of single atom magnets on graphene, Nano Lett. **16**, 7610 (2016).

[26] T. Miyamachi, T. Schuh, T. Märkl, T. Bresch, C.and Balashov, A. Stöhr, C. Karlewski, S. André, M. Marthaler, M. Hoffmann, S. Geilhufe, M. ans Ostanin, W. Hergert, I. Mertig, G. Schön, A. Ernst, and W. Wulfhekel, Stabilizing the magnetic moment of single Holmium atoms by symmetry, Nature (London) **503**, 242 (2013).

[27] A. Herman, S. Kraus, S. Tsukamoto, L. Spieker, V. Caciuc, T. Lojewski, D. Günzing, J. Dreiser, B. Delley, K. Ollefs, T. Michely, N. Atodiresei, and H. Wende, Tailoring magnetic anisotropy by graphene-induced selective Skyhook effect on $4f$-metals, Nanoscale **14**, 7682 (2022).

[28] L. Peters, I. Di Marco, P. Thunström, M. I. Katsnelson, A. Kirilyuk, and O. Eriksson, Treatment of $4f$ states of the rare earths: The case study of TbN, Phys. Rev. B **89**, 205109 (2014).

[29] A. B. Shick, D. S. Shapiro, J. Kolorenc, and A. I. Lichtenstein, Magnetic character of holmium atom adsorbed on platinum surface, Sci. Rep. **7**, 2751 (2017).

[30] A. B. Shick and A. Y. Denisov, Magnetism of $4f$-atoms adsorbed on metal and graphene substrates, J. Magn. Magn. Mater. **475**, 211 (2019).

[31] A. B. Shick, J. Kolorenč, A. I. Lichtenstein, and L. Havela, Electronic structure and spectral properties of Am, Cm, and Bk: Charge-density self-consistent LDA + HIA calculations in the FP-LAPW basis, Phys. Rev. B **80**, 085106 (2009).

[32] K. Held, Electronic structure calculations using dynamical mean field theory, Adv. Phys. **56**, 829 (2007).

[33] V. I. Anisimov, F. Aryasetiawan, and A. Lichtenstein, First-principles calculations of the electronic structure and spectra of strongly correlated systems: The LDA + U method, J. Phys.: Condens. Matter **9**, 767 (1997).

[34] A. B. Shick, A. I. Liechtenstein, and W. E. Pickett, Implementation of the LDA + U method using the full-potential linearized augmented plane-wave basis, Phys. Rev. B **60**, 10763 (1999).

[35] https://www.flapw.de/

[36] D. Wortmann, G. Michalicek, N. Baadji, M. Betzinger, G. Bihlmayer, J. Bröder, T. Burnus, J. Enkovaara, F. Freimuth, C. Friedrich, C.-R. Gerhorst, S. Granberg Cauchi, U. Grytsiuk, A. Hanke, J.-P. Hanke, M. Heide, S. Heinze, R. Hilgers, H. Janssen, D. A. Klüppelberg *et al.*, FLEUR, Zenodo (2023), https://doi.org/10.5281/zenodo.7891361.

[37] M. Jugovac, I. Cojocariu, J. Sánchez-Barriga, P. Gargiani, M. Valvidares, V. Feyer, S. Blügel, G. Bihlmayer, and P. Perna, Inducing single spin-polarized flat bands in monolayer graphene, Adv. Mater. **35**, 2301441 (2023).

[38] D. F. Förster, T. O. Wehling, S. Schumacher, A. Rosch, and T. Michely, Phase coexistence of clusters and islands: Europium on graphene, New J. Phys. **14**, 023022 (2012).

[39] C. Li, A. J. Freeman, H. J. F. Jansen, and C. L. Fu, Magnetic anisotropy in low-dimensional ferromagnetic systems: Fe monolayers on Ag(001), Au(001), and Pd(001) substrates, Phys. Rev. B **42**, 5433 (1990).

[40] J. P. Perdew, K. Burke, and M. Ernzerhof, Generalized gradient approximation made simple, Phys. Rev. Lett. **77**, 3865 (1996).

[41] D. van der Marel and G. A. Sawatzky, Electron-electron interaction and localization in d and f transition metals, Phys. Rev. B **37**, 10674 (1988).

[42] I. L. M. Locht, Y. O. Kvashnin, D. C. M. Rodrigues, M. Pereiro, A. Bergman, L. Bergqvist, A. I. Lichtenstein, M. I. Katsnelson, A. Delin, A. B. Klautau, B. Johansson, I. Di Marco, and O. Eriksson, Standard model of the rare earths analyzed from the Hubbard I approximation, Phys. Rev. B **94**, 085137 (2016).

[43] B. Dorado, B. Amadon, M. Freyss, and M. Bertolus, DFT + U calculations of the ground state and metastable states of uranium dioxide, Phys. Rev. B **79**, 235125 (2009).

[44] J. P. Allen and G. W. Watson, Occupation matrix control of d- and f-electron localisations using DFT + U, Phys. Chem. Chem. Phys. **16**, 21016 (2014).

[45] X. Liu, C. Z. Wang, M. Hupalo, W. C. Lu, M. C. Tringides, Y. X. Yao, and K. M. Ho, Metals on graphene: Correlation between adatom adsorption behavior and growth morphology, Phys. Chem. Chem. Phys. **14**, 9157 (2012).

[46] V. A. Basiuk, O. V. Prezhdo, and E. V. Basiuk, Adsorption of lanthanide atoms on graphene: Similar, yet different, J. Phys. Chem. Lett. **13**, 6042 (2022).

[47] M. T. Hutchings, Point-charge calculations of energy levels of magnetic ions in crystalline electric fields, in *Solid State Physics*, edited by F. Seitz and D. Turnbull (Academic Press, New York, London, 1964), Vol. 16, pp. 227–273.

[48] R. Skomski, P. Manchanda, and A. Kashyap, Anisotropy and crystal field, in *Handbook of Magnetism and Magnetic Materials* (Springer International Publishing, Cham, 2020).

[49] M. Kuz'min and A. Tishin, Theory of crystal-field effects in 3d-4f intermetallic compounds, Handb. Magn. Mater. **17**, 149 (2007).

[50] R. Radwański and J. Franse, Magnetocrystalline anisotropy and crystal field in Ho_2Co_{17}, Phys. B: Condens. Matter **154**, 181 (1989).

[51] K. Stevens, Matrix elements and operator equivalents connected with the magnetic properties of rare earth ions, Proc. Phys. Soc. Sect. A **65**, 209 (1952).

[52] C. E. Patrick, G. A. Marchant, and J. B. Staunton, Spin orientation and magnetostriction of $Tb_{1-x}Dy_xFe_2$ from first principles, Phys. Rev. Appl. **14**, 014091 (2020).

[53] M. Yamada, H. Kato, H. Yamamoto, and Y. Nakagawa, Crystal-field analysis of the magnetization process in a series of $Nd_2Fe_{14}B$-type compounds, Phys. Rev. B **38**, 620 (1988).

[54] D. Gatteschi and R. Sessoli, Quantum tunneling of magnetization and related phenomena in molecular materials, Angew. Chem., Int. Ed. **42**, 268 (2003).

[55] S. Schumacher, F. Huttmann, M. Petrović, C. Witt, D. F. Förster, C. Vo-Van, J. Coraux, A. J. Martínez-Galera, V. Sessi, I. Vergara, R. Rückamp, M. Grüninger, N. Schleheck, F. Meyer zu Heringdorf, P. Ohresser, M. Kralj, T. O. Wehling, and T. Michely, Europium underneath graphene on Ir(111): Intercalation mechanism, magnetism, and band structure, Phys. Rev. B **90**, 235437 (2014).

[56] S. Abdelouahed, N. Baadji, and M. Alouani, Electronic structure and x-ray magnetic circular dichroism of Gadolinium beyond the local spin density approximation, Phys. Rev. B **75**, 094428 (2007).

[57] S. Jiang and S. Qin, Prediction of the quantized axis of rare-earth ions: The electrostatic model with displaced point charges, Inorg. Chem. Front. **2**, 613 (2015).

[58] J. Sievers, Asphericity of 4f-shells in their Hund's rule ground states, Z. Phys. B **45**, 289 (1982).

[59] S. Kraus, A. Herman, F. Huttmann, C. Kramer, K. Amsharov, S. Tsukamoto, H. Wende, N. Atodiresei, and T. Michely, Selecting the reaction path in on-surface synthesis through the electron chemical potential in graphene, J. Am. Chem. Soc. **144**, 11003 (2022).

[60] F. Huttmann, A. J. Martínez-Galera, V. Caciuc, N. Atodiresei, S. Schumacher, S. Standop, I. Hamada, T. O. Wehling, S. Blügel, and T. Michely, Tuning the van der Waals interaction of graphene with molecules via doping, Phys. Rev. Lett. **115**, 236101 (2015).

[61] S. Schumacher, T. O. Wehling, P. Lazic, S. Runte, D. F. Förster, C. Busse, M. Petrovic, M. Kralj, S. Blügel, N. Atodiresei, V. Caciuc, and T. Michely, The backside of graphene: Manipulating adsorption by intercalation, Nano Lett. **13**, 5013 (2013).

[62] J. Cenker, S. Sivakumar, K. Xie, A. Miller, P. Thijssen, Z. Liu, A. Dismukes, J. Fonseca, E. Anderson, X. Zhu, X. Roy, D. Xiao, J. Chu, T. Cao, and X. Xu, Reversible strain-induced magnetic phase transition in a van der Waals magnet, Nat. Nanotechnol. **17**, 256 (2022).

[63] D. Jiles and C. Lo, The role of new materials in the development of magnetic sensors and actuators, Sens. Actuators, A **106**, 3 (2003).

[64] X. Hu, X. Zhao, Y.and Shen, A. V. Krasheninnikov, Z. Chen, and L. Sun, Enhanced ferromagnetism and tunable magnetism in Fe_3GeTe_2 monolayer by strain engineering, ACS Appl. Mater. Interfaces **12**, 26367 (2020).

[65] A. L. Kozub, A. B. Shick, F. Máca, J. Kolorenč, and A. I. Lichtenstein, Electronic structure and magnetism of samarium and neodymium adatoms on free-standing graphene, Phys. Rev. B **94**, 125113 (2016).

[66] P. M. Morse, Diatomic molecules according to the wave mechanics. II. Vibrational levels, Phys. Rev. **34**, 57 (1929).

[67] V. I. Minkin, Glossary of terms used in theoretical organic chemistry, Pure Appl. Chem. **71**, 1919 (1999).